




Pore-corner networks unveiled: Extraction and interactions in porous mediaNinghua Zhan ^{1,2}, Yiping Wang,³ Xiang Lu,² Rui Wu ^{1,*} and Abdolreza Kharaghani ²¹*School of Mechanical Engineering, Shanghai Jiao Tong University, Shanghai 200240, China*²*Chair of Thermal Process Engineering, Otto von**Guericke University, P.O. 4120, 39106 Magdeburg, Germany*³*Exploration and Development Research Institute of Shengli Oilfield Company, Sinopec, Dongying, 257000 Shandong, China*

(Received 10 August 2023; accepted 8 December 2023; published 17 January 2024)

Generalized network models (GNMs) serve as powerful tools, bridging the intricate gap between pore- and continuum-scale multiphase transport in porous media. An essential step in the development of these models is to extract pore-corner networks from actual porous materials. In this paper, we present a pore-corner-network extraction method involving two steps. In the first step, pore networks, comprising pore bodies interconnected by pore throats, are extracted based on the omnidirectional Euclidean distance concept. Subsequently, corners within each distinct pore unit, consisting of a pore body and half of the connected pore throats, are identified by sweeping the pore unit with a sphere. The radius of the sphere corresponds to the minimal corner radius within the cross-sections at the centers of pore throats within the pore unit. To extract pore-corner networks from three-dimensional images of porous materials efficiently, we introduce a domain decomposition approach. In this approach, the porous material of interest is divided into multiple subdomains, each enveloped by a protective layer. To validate our proposed extraction method, a GNM is developed to simulate evaporation in a porous medium composed of packed spherical beads. This model is systematically compared with microcomputed tomography experimental data. Encouragingly, the modeling results are in good agreement with the experimental data, particularly in terms of the variation of liquid distribution over time. Our proposed extraction method not only contributes to disclosing the structures of pores and corners in real porous media but also benefits the development of GNMs that can be employed to understand in detail the multiphase transport in porous media from the pore-scale perspectives.

DOI: [10.1103/PhysRevFluids.9.014303](https://doi.org/10.1103/PhysRevFluids.9.014303)**I. INTRODUCTION**

Multiphase transport in porous media is of great interest not only to scientific researchers but also to many industrial applications. This includes areas such as oil recovery [1,2], subsurface carbon dioxide and hydrogen storage [3,4], as well as proton exchange membrane fuel cells and electrolyzers [5,6]. Despite its relevance, an accurate depiction of multiphase transport in porous media remains challenging due to its inherently multiscale nature. The dynamics of interfaces between different fluids within the pores of porous materials, exemplified by phenomena such as capillary valve effects [7,8] and capillary instability effects [9], exert control over multiphase transport processes at the continuum scale, i.e., at the scale of at least several representative elementary volumes (REV)s. Thus, to depict the multiphase transport in porous media accurately, it

*Corresponding author: ruiwu@sjtu.edu.cn

is necessary to link the interfacial dynamics and the continuum-scale transport processes. This issue, however, is difficult to address experimentally since the resolution and the size of view field cannot be satisfied simultaneously. Numerically, direct numerical simulations, e.g., volume of fluid (VOF) [10] and the lattice Boltzmann method (LBM) [11], are aimed at cases of small computational domains, whereas in continuum models, the pore structures and the interfacial dynamics at the pore scale are not considered explicitly [12]. By contrast, generalized network models (GNMs) have a good tradeoff between the depiction of the interfacial dynamics and the computational efficiency [13].

In the GNMs, the void space of a porous material is conceptualized as a pore network composed of large regular pore bodies connected by small regular pore throats, or the void space is taken as a pore-corner network composed of not only pore bodies and pore throats but also the corners in each pore body and each pore throat to consider the transport of fluids in corner films. The transport of fluid in each pore and each corner is depicted as a one-dimensional (1D) process. The interfaces between different fluids in pores and corners are assumed spherical; thus, the interface reconstruction, e.g., needed in VOF, is avoided. Because of these treatments, GNMs can model multiphase transport in porous media with sizes of several REV's and at a lower capillary number than the direct numerical simulations. Thus, GNMs are the ideal approach to link the multiphase interfacial dynamics in pores and corners in porous media and the macroscale multiphase transport processes [14].

The accuracy of GNMs is determined by the algorithm depicting the transport of fluid in each pore and corner as well as the pore and/or pore-corner networks extracted from real porous media. The microstructures of porous media play an important role in controlling multiphase transport processes, especially the fluids residing in the corners of pores, referred to as corner films, as observed in various studies [15–17]. In the context of evaporation, the corner liquid films provide paths for liquid transport to the surfaces of porous media, hence impacting the evaporation rate. The precise prediction of the evaporation rate from porous media, where corner liquid films play a critical role, has garnered considerable attention [18–20]. Over the past two decades, substantial efforts have been devoted to the development of GNMs incorporating corner liquid films for porous media evaporation [21–31]. While notable progress has been made in modeling evaporation with corner liquid films in specific geometries like capillary tubes with square cross-sections [32,33] and quasi-two-dimensional (quasi-2D) microfluidic pore networks [30], achieving accurate GNMs for depicting evaporation in real three-dimensional (3D) porous media, such as the evaporation rate and capillary liquid rings in the corners of sphere packing, remains a challenge [29,31]. Addressing this challenge requires the extraction of accurate pore-corner networks from real porous media, a task crucial not only for advancing GNMs but also for refining techniques to characterize the topologies of pores and corners in real porous materials.

To extract pore-corner networks, the pore network structures are needed first; then the corners in each pore throat and each pore body of the pore network are determined. The ideas for the pore-network extraction are as follows. First, the porous material of interest is voxelized. Then the hierarchy of the void voxels is determined by the Euclidean distance (ED) [34,35] or the more accurate omnidirectional ED (OED) method [36]. After this, the pore network composed of pore bodies connected by pore throats is extracted to mimic the pore space of the voxelized porous material. The maximal ball (MB) [37–39], watershed segmentation (WS) [40–45], and medial axis (MA) [46–51] are the three methods widely employed for pore-network extraction. Each extraction methodology has its own advantages and flaws. The different extraction methods have also been combined to employ the advantages of various extraction methods, e.g., Refs. [52,53].

Once the pore networks are gained, the corners in each pore body and each pore throat need to be extracted to construct the pore-corner networks. A method proposed by Raeini *et al.* [13] outlines the corner extraction process as follows: Firstly, MAs of the pore throat surfaces are generated. Then each branch of the MAs is assigned a corner label. Finally, these corner labels from the throat MAs are mapped to the underlying image and then grown toward the pore-body centers. That is to say, in the method proposed in Ref. [13], corners on a 2D pore-throat surface (cross-section) are extended

to encompass the whole 3D void space between the pore bodies connected by that pore throat; this, on the other hand, implies that the cross-sections between these two pore bodies have the same number of corners. Nevertheless, real porous media have complex pore and corner structures, and the structures of corners at two cross-sections between two adjacent pore bodies can be completely different; see Fig. S1 in the Supplemental Material [54] for more details.

In this paper, an alternative extraction method is proposed to gain the accurate pore-corner networks from real porous media. We first determine the pore bodies and pore throats using our proposed OED-based pore-network extraction method [36]. A pore unit is composed of a pore body and half of the connected pore throats. The corner radius of a pore throat is determined as the radius of the residual wetting phase after drainage of the cross-section perpendicular to the MA and located at the pore-throat center. The corner radius of a pore unit is equal to the smallest corner radius of the pore throat in this pore unit. Then the corners in each pore unit are determined by sweeping this pore unit with a sphere with the radius equal to the corner radius of this pore unit. After this, pore-corner networks are extracted. To validate our proposed extraction method, we develop a GNM based on this extraction method to model the evaporation from packing of spherical beads. The modeling results are in good agreement with the experimental data in terms of the variation of the liquid distribution with time. Especially, the experimentally observed capillary rings formed by the liquid corner films are successfully captured by our developed GNM. The agreement between the GNM and experimental results demonstrates the effectiveness of our proposed method to extract pore-corner networks from real porous media.

The paper is organized as follows. In Sec. II, the workflow of the proposed pore-corner-network extraction is introduced. In Sec. III, the OED-based pore-network extraction is briefly introduced. In Sec. IV, the method to determine corners in each pore throat and pore body is presented. In Sec. V, the domain decomposition technology is introduced to extract pore-corner networks from voxelized porous media of large size. Based on the proposed pore-corner-network extraction method, a GNM is developed for the evaporation of sphere packing in Sec. VI, and the modeling and experimental results are compared. Finally, Sec. VII concludes the paper, summarizing the insights drawn from the study.

II. WORKFLOW OF PORE-CORNER-NETWORK EXTRACTION

In our proposed method for extracting pore-corner networks, the initial step involves determining the MAs of the void space of the voxelized porous material of interest as well as identifying the pore-throat and pore-body regions by using the OED-based pore-network extraction method presented in our previous study [36]. Then the corners in each pore throat and pore body of the extracted pore network are identified, thereby forming the pore-corner network.

An important element of our corner determination approach is the identification of corner radii for pore units. Each pore unit is composed of a pore body and the void space between this pore body and the centers of neighboring pore throats, i.e., half of the connected pore throats. Subsequently, we determine the corner radius for each cross-section that is perpendicular to each MA, located at the center of each pore throat. The computation of the corner radius relies on the semianalytical method proposed by Frette and Helland [55], specifically for the corner radius of a pore throat. After this, the corner radii of all pore throats in each pore unit are determined. The corner radius of each pore unit is defined as the smallest corner radius among the pore throats in that pore unit. Each pore unit is then traversed by a sphere with a radius equal to the corner radius of that specific pore unit. Void voxels in each pore unit that cannot be swept by the sphere are determined as corners. In this way, corners in each pore unit can be determined. The overall process of pore-corner-network extraction includes two key steps: pore-network extraction, followed by corner-network extraction, as illustrated in Fig. 1. Figure 1(a) shows the pore structure of a porous material composed of packed spheres (the sphere packing is illustrated in Fig. S2 in the Supplemental Material [54]). Figures 1(b) and 1(c) show the MAs as well as the pore-body regions and the pore-throat region

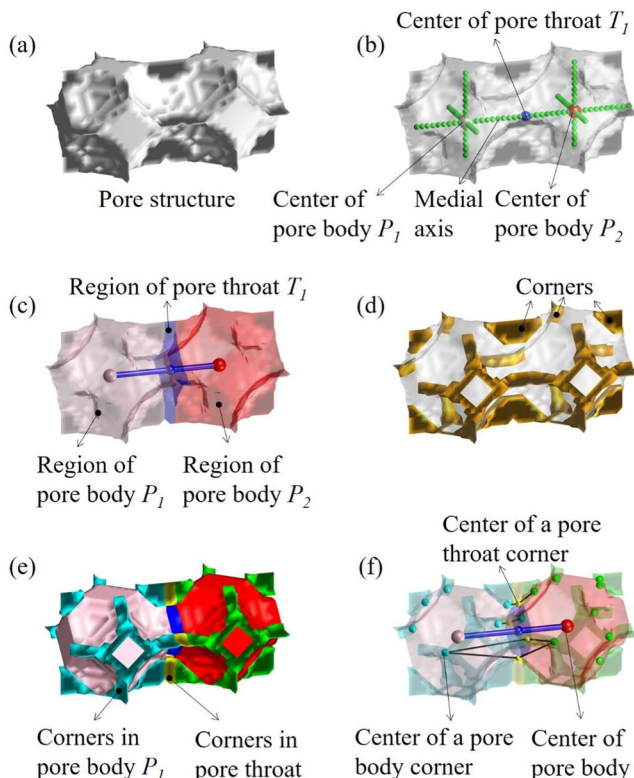


FIG. 1. Steps to extract a pore-corner network. (a) Void space of 12 packed spheres illustrated in Fig. S2 in the Supplemental Material [54]. (b) Medial axis of the void space. (c) Regions of pore bodies and of pore throats. (d) Extraction of corners in void space. (e) Identification of corners in pore bodies and pore throats. (f) Extracted pore-corner network.

in the pore-network extraction. Figures 1(d) and 1(e) illustrate the corners in the corner-network extraction. Finally, Fig. 1(f) presents the extracted pore-corner network.

In Fig. 1(f), the larger light pink, red, and blue spheres represent the centers of pore bodies and pore throats, respectively. The blue cylinders denote the interconnection between the pore bodies and the pore throats. The smaller light blue, green, and yellow spheres represent the centers of corners in within pore bodies and pore throats. The interconnectivity between these pore corners is illustrated through black lines. The light blue corners are in the pink pore body, the green corners are in the red pore body, and the yellow corners are in the blue pore throat.

The comprehensive process of pore-network extraction and corner-network extraction, as illustrated in Fig. 1, is introduced in detail in the following sections.

III. PORE-NETWORK EXTRACTION

The extraction of pore networks of porous media is accomplished through our proposed OED-based extraction method, as detailed in our previous work [36]. A concise overview of the steps of the method is briefly outlined here and complemented by a visual representation in Fig. 2:

(1) The initial step encompasses determining the anchored void voxels situated at the inlet and outlet surfaces of the voxelized porous medium [e.g., as depicted in Fig. 2(a)]. These anchored void voxels, illustrated in yellow in Fig. 2(b), are determined through an approach which is different from

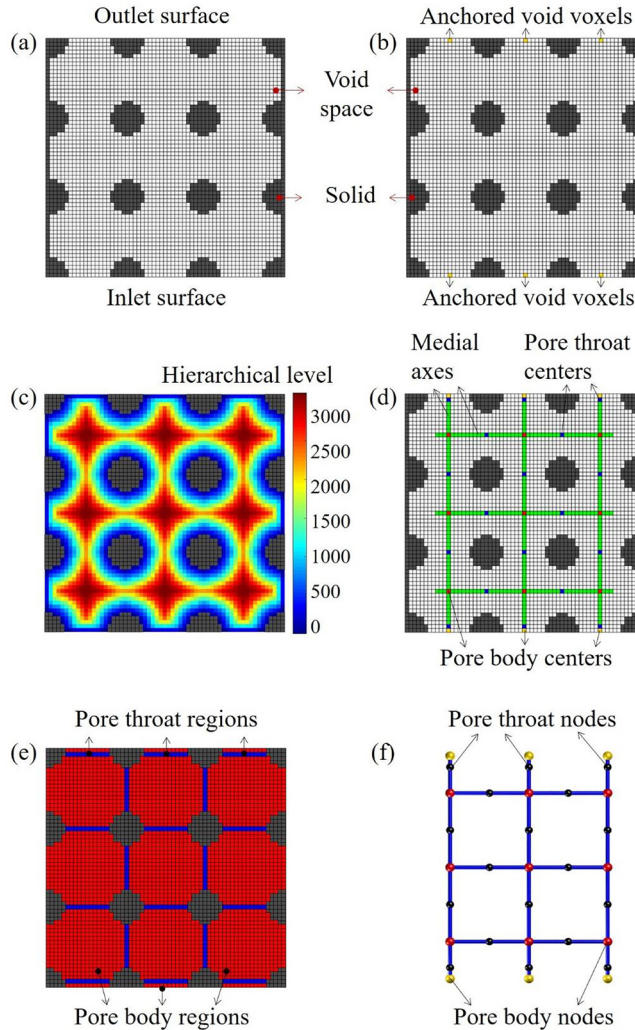


FIG. 2. Steps to extract a pore network from a two-dimensional (2D) porous medium. (a) A 2D voxelized porous medium. (b) The anchored void voxels at the inlet and outlet surfaces of the medium. (c) Hierarchical levels of void voxels inside the voxelized porous medium. (d) Medial axis and the centers of pore bodies and of pore throats. (e) Pore-body regions (shown in red) and pore-throat regions (shown in blue). (f) Extracted pore network.

that in Ref. [36]. The details of this approach are pointed out in the following paragraphs. Their role is vital in establishing nonsimple void voxels inside the voxelized porous medium; see step (3).

(2) The next step is computing the OED for each void voxel inside the voxelized porous medium. This computation leads to the establishment of a hierarchical arrangement of void voxels, illustrated in Fig. 2(c). The hierarchical order of the OED assigned to each void voxel is termed as its hierarchical level.

(3) The nonsimple void voxels inside the voxelized porous medium are determined by the omnidirectional distance order homotopic thinning (ODOHT) algorithm. These nonsimple void voxels inside the voxelized porous medium, combined with the anchored void voxels at the inlet and outlet surfaces, collectively form the MAs of the void space, as visualized by green lines in

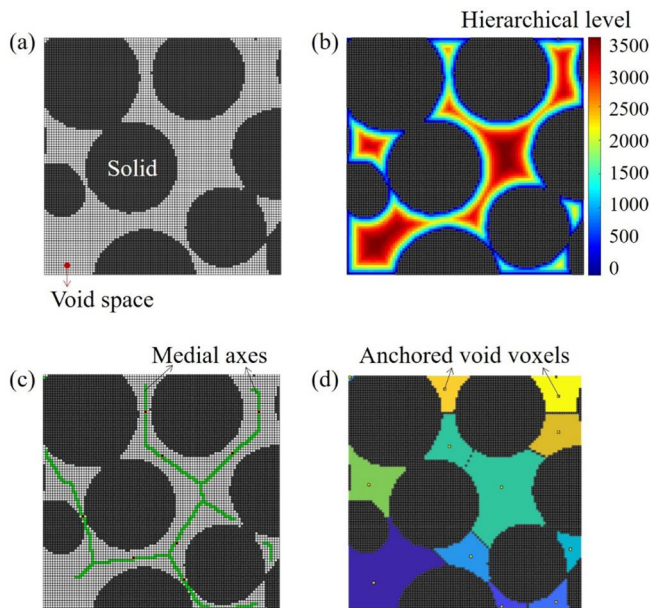


FIG. 3. Steps to obtain the anchored void voxels at the inlet and/or outlet surfaces of porous media. (a) The inlet and/or outlet surface of a porous material composed of packed spheres. (b) Hierarchical levels of void voxels. (c) Extracted medial axes (green lines) and the neck void voxels (black voxels). (d) Void clusters and the anchored void voxels (yellow voxels).

Fig. 2(d). The pore-body centers (void voxels in red) and the pore-throat centers (void voxels in blue) at the MAs are determined. Note that the anchored void voxels at the inlet and outlet surfaces are considered pore-body centers.

(4) The pore-body and pore-throat regions are determined, as illustrated in Fig. 2(e). In this way, the pore network composed of nodes connected by bonds is extracted; see Fig. 2(f). The nodes represent the centers of pore bodies and/or of pore throats. A bond between two nodes depicts the connection between a pore body and its adjacent pore throat. For the pore network shown in Fig. 2(f), two pore bodies are connected by only one pore throat. However, it is noteworthy that, in real 3D porous media, the connectivity between two pore bodies can involve multiple pore throats—refer to our previous work for more comprehensive details [36].

This systematic sequence of steps collectively constitutes the process of pore-network extraction, comprehensively illustrated and summarized in Fig. 2.

In our previous study [36], the pore-network extraction of a porous medium composed of stacked cylindrical fibers was explored. The fibers in such digital porous material can overlap with each other, resulting in void spaces at the inlet and/or outlet surfaces being segmented into several void clusters that are separated by the solid matrix, as illustrated in Fig. S3 in the Supplemental Material [54]. In each void cluster, the void voxel with the highest hierarchical level is defined as the anchored one. However, for porous media composed of packed spheres, e.g., the one introduced in the following Sec. V, most of the void voxels at the inlet and/or outlet surface are connected to each other, e.g., see the voxelized surface with 100×100 voxels shown in Fig. 3(a). Thus, our approach in this work diverges from that outlined in Ref. [36], necessitating an alternative method for determining anchored void voxels at the inlet and/or outlet surfaces, as illustrated in Fig. 3. Here is the refined methodology:

(1) The OED of each void voxel at the inlet or outlet surface is calculated, considering a 2D ED from a void voxel to a solid boundary voxel in the same surface. Based on the computed OED, the hierarchical levels of void voxels are determined, illustrated in Fig. 3(b).

(2) Based on the hierarchical levels of void voxels, the MAs in the surface are determined by the ODOHT algorithm, illustrated by the green lines in Fig. 3(c).

(3) The void voxel of the minimum hierarchical level in each MA is determined and termed as the potential neck void voxel, denoted by the black points in Fig. 3(c). However, potential neck void voxels situated at the end of a MA are excluded from this consideration. Additionally, if the distance between two potential neck void voxels falls below a critical threshold (e.g., 3 voxels in this paper), only the lower hierarchical level is retained as the designated neck void voxel.

(4) The void space of the surface is segmented into several void clusters by introducing lines that intersect the neck void voxels and are perpendicular to the corresponding MAs, as exemplified in Fig. 3(d). In each void cluster, the void voxel with the maximum hierarchical level is selected as the anchored voxel, highlighted as the yellow void voxel in Fig. 3(d). These anchored void voxels at the inlet and outlet surfaces play a pivotal role in identifying nonsimple void voxels inside porous media, as we mentioned previously.

IV. CORNER-NETWORK EXTRACTION

After the pore network has been successfully extracted, the subsequent steps involve determining the corners within each pore throat and each pore body. Precise defining the corners of a void space presents a geometric challenge, yet describing their structural attributes is vital for understanding two-phase transport phenomena in porous media. For instance, for drainage, i.e., a nonwetting fluid displaces a wetting fluid, in a porous material, the wetting fluid can reside in the corners of a pore after this pore is invaded by the nonwetting fluid. From the perspective of two-phase transport in porous media, we can define the zones occupied by the wetting fluid following drainage within a pore as its corners. The extent of wetting fluid volume within these corners after drainage depends on the wettability of the pore wall, reaching its maximum when the contact angle of the wall surface is zero. The contact angle is the angle between the interface of the wetting and nonwetting fluids and the interface of the wetting fluid and solid. Thus, one way to determine the corners in each pore in an extracted pore network is to model the drainage in each pore body and each pore throat. This approach, however, is time consuming.

The drainage process in a single-entry, single-exit pore throat can be decomposed into successive drainage of a series of cross-sections of the pore throat along the MA. Thus, the threshold pressure for the breakthrough of nonwetting fluid within this pore throat aligns with that required for the invasion of its narrowest cross-section. This threshold pressure is related to the radius of the wetting fluid films r_{film} , which remains at the corners of this minimal cross-section. Specifically, when the contact angle is zero, this threshold pressure equates to σ/r_{film} .

All the wetting fluid films have the same value as the ones at the narrowest cross-section after the breakthrough of the nonwetting fluid in the pore throat. The radius of the wetting fluid films at the corners of a 2D cross-section of a pore can be determined quickly by the semianalytical approach proposed by Frette and Helland [55]. Thus, the corners in a pore throat can be determined quickly by determining the radius of the wetting fluid films at the corners of the narrowest cross-section. This radius is called the corner radius of this pore throat. Similarly, the corners in a pore unit composed of a pore body and half of the connected pore throats, i.e., void space between this pore body and centers of neighboring pore throats, can be determined by the smallest radius of wetting fluid films at the corners of the narrowest cross-section in these connected pore throats (this radius is called the corner radius of the pore unit).

Based on the above analysis, we propose the following procedure to determine the corners in a pore unit, as illustrated in Fig. 4 [the structure of a pore unit is shown in Fig. 4(a)]. Firstly, the 2D cross-section of each pore throat, i.e., the plane perpendicular to MA and at the center of each pore throat, is determined, Fig. 4(b). Secondly, the corner radius for the 2D cross-section of each pore throat (i.e., the so-called corner radius of the pore throat) is determined, which is equal to the radius of the interface between the wetting and nonwetting fluids in this cross-section after invasion by the nonwetting fluid, as r_{film} shown in Fig. 4(b). Note that the wetting fluids in the corners form

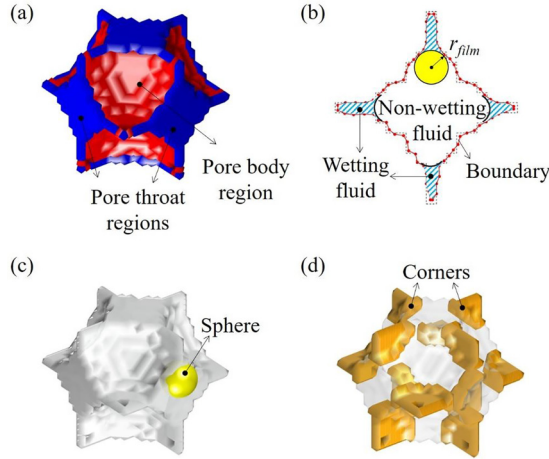


FIG. 4. Steps to extract corners in a pore unit: (a) The structure of a pore unit composed of a pore body (red zone) and void space between this pore body and centers of neighboring pore throats (blue zones). (b) Corner radius of the two-dimensional (2D) cross-section of a pore throat. (c) The pore unit (shown in white) is swept by a sphere (shown in yellow) with the radius equal to corner radius of this pore unit. (d) Extracted corners (orange zone) in the pore unit.

the so-called corner films. Thirdly, the smallest corner radius of the pore throat in the pore unit is determined, which is called the corner radius of this pore unit. Finally, the corners in the pore unit are determined by sweeping the pore unit with a sphere of the radius equal to the corner radius of this pore unit, Figs. 4(c) and 4(d). The details of these steps are presented below.

A. Cross-section of pore throat

As previously mentioned, the cross-section of a pore throat is determined by the plane positioned at the center of this pore throat. This plan is oriented perpendicular to the MA of the pore throat. The cross-section obtained by this method has a 3D topological structure. However, to gain the corner radius of a pore throat introduced in Fig. 4(b) as well as in the following paragraphs, the 3D cross-section at the center of this pore throat needs to transform into a 2D one. Figure 5(a) shows the 3D cross-sectional view situated at the center of a pore throat depicted in Fig. 4(a). The void voxel at the center of this pore throat $P_0(x_0, y_0, z_0)$ is also considered the center of this 3D cross-section; here, x_0 , y_0 , and z_0 are the coordinates of void voxel P_0 . The void voxel in this 3D cross-section that stands farthest from $P_0(x_0, y_0, z_0)$ is identified as $P_a(x_a, y_a, z_a)$. The axis connected by $P_0(x_0, y_0, z_0)$ and $P_a(x_a, y_a, z_a)$ is called the main axis. For any given void voxel positioned in this 3D

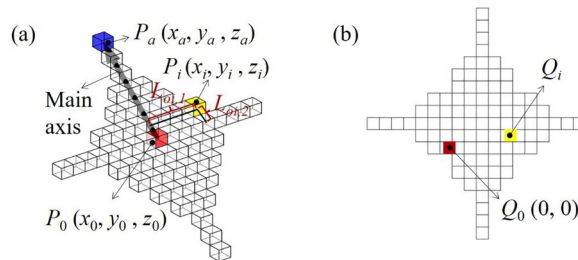


FIG. 5. Schematic of the transformation of (a) a three-dimensional (3D) cross-section into (b) a two-dimensional (2D) representation at the center of a pore throat.

cross-section—denoted as $P_i(x_i, y_i, z_i)$ —its distance to the main axis is denoted by $L_{oi,1} = \frac{|\vec{P}_0\vec{P}_i \times \vec{P}_0\vec{P}_a|}{|\vec{P}_0\vec{P}_a|}$, and its distance to $P_0(x_0, y_0, z_0)$ parallel to the main axis direction is $L_{oi,2} = \frac{|\vec{P}_0\vec{P}_i \cdot \vec{P}_0\vec{P}_a|}{|\vec{P}_0\vec{P}_a|}$.

The following procedure is employed to transform a 3D cross-section into a 2D representation. First, the center of the 2D cross-section is defined as $Q_0(0, 0)$, as illustrated in Fig. 5(b). Then any void voxel in the 3D cross-section $P_i(x_i, y_i, z_i)$ is determined as $Q_i[\text{round}_L(L_{oi,1}), \text{round}_L(L_{oi,2})]$ in the 2D cross-section, for which round_L is a function to round a real number to a lower nearest integer. In this way, the 2D cross-section of each pore throat is gained which, however, has a jagged discrete boundary. Such a discrete boundary cannot represent the true boundary accurately. Hence, it is needed to reconstruct a real boundary based on information of the discrete boundary of the 2D cross-section. To do this, the method proposed in Ref. [56] is employed, in which the Euclidean paths of the discrete boundary are gained to approximate the real boundary. The details of this method can be found in Refs. [56,57] and hence are not repeated here. The constructed Euclidean paths of the cross-section in Fig. 5(b) are shown as the red line in Fig. 4(b).

B. Corner radius of pore throat

After the 2D cross-section with Euclidean paths (to approximate the real boundary) of each pore throat is obtained, the subsequent steps involve simulating the invasion of a nonwetting fluid into each of these 2D cross-sections. Initially, these cross-sections are filled with a wetting fluid, and this invasion process is orchestrated by utilizing the semianalytical method proposed in Ref. [55]. In this modeling, the contact angle is assumed to be zero, thereby maximizing the volume of corners within the pore throat. In this way, we can obtain the threshold pressure for invasion of the nonwetting fluid and the configuration of the wetting fluid as well as the radius of the interface between the wetting and nonwetting fluids in the 2D cross-section of each pore throat [the wetting fluid resides in the corners, forming the corner films, as illustrated in Fig. 4(b)]. This radius is called the corner radius of the pore throat.

C. Corner network

After the corner radius of each pore throat is obtained, the next step is to determine the corners in each pore body and pore throat. This process unfolds as follows: The void space is divided into lots of pore units. The corner radius of a pore unit is equal to the smallest corner radius of pore throat inside this pore unit. The corners in a pore unit are determined by sweeping this pore unit with a sphere with the radius equal to the corner radius of this pore unit, as illustrated in Fig. 4(c). The void voxels in the pore unit are considered corner void voxels if the centers of these void voxels are not touched by the sweeping sphere. In this way, the corner void voxels in each pore body and each pore throat are determined, as illustrated in Fig. 6(a).

After the corner void voxels are determined, we then identify the clusters of corner void voxels in each pore body and each pore throat by using the Hoshen-Kopelman algorithm proposed in Ref. [58], as illustrated in Fig. 6(b). A cluster of corner void voxels in a pore (pore body or pore throat) is composed of corner void voxels connected to each other in this pore. A corner represents the corner void voxels only in a pore body or in a pore throat. For each corner, the OED of void voxels is determined, and the hierarchical levels are obtained, e.g., see the void voxels in the pore throat corners shown in Fig. 6(c). The hierarchical levels of void voxels in the pore body corners are shown in Fig. S4 in the Supplemental Material [54]. For each corner, the void voxel of highest hierarchical level is taken as the center of this corner; see the spheres in Fig. 6(d). If a void voxel in a corner is in contact with a void voxel in a corner in a different pore, then these two corners in different pores (e.g., in a pore throat and a pore body) are connected; see the spheres connected by black lines in Fig. 6(d). In this way, the corner network, i.e., the network composed of corners, can be extracted, as illustrated in Fig. 6(d). Examples of corner extraction from more complicated pore structures can be found in Fig. S1 in the Supplemental Material [54].

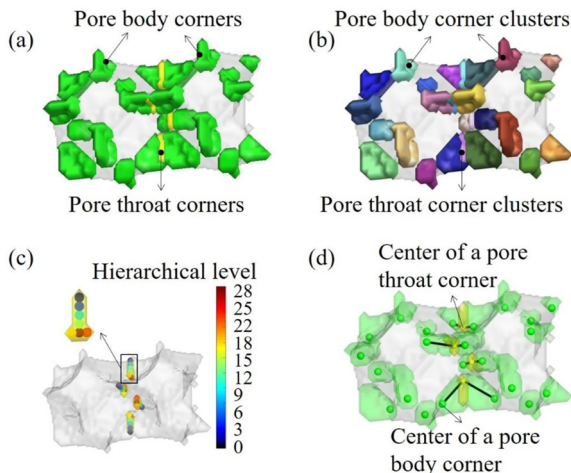


FIG. 6. Steps to extract a corner network. (a) Corner void voxels in pores (shown in green in the pore bodies and yellow in the pore throat). (b) Clusters of corner void voxels. (c) Omnidirectional Euclidean distance (OED) of corner void voxels in the pore throat. (d) Extracted corner network.

V. EXTRACTION OF A PORE-CORNER NETWORK FROM A LARGE POROUS MEDIUM

Based on the pore-network extraction approach introduced in Sec. III and the corner-network extraction approach introduced in Sec. IV, the pore-corner networks of porous media now can be extracted straightforwardly. In our method proposed for pore-corner-network extraction, a crucial step involves determining the OED of each void voxel as well as the MAs in a digital porous medium. The OED of a void voxel is determined by calculating the distance from that void voxel to all accessible solid voxels. A solid voxel is considered accessible to a void voxel if a line connecting them is uninterrupted by any other solid voxels. Thus, as the size of the digital porous medium (e.g., the number of voxels) increases, the overall memory and CPU time required for determining the OEDs of void voxels and the MAs can significantly increase. To mitigate such computational costs, the domain of the digital porous medium of interest is partitioned into several subdomains using the domain decomposition method, as illustrated in Fig. 7(a). In this depiction, a 2D digital porous medium with 100×100 voxels is divided into four subdomains, each containing 50×50 voxels.

Hence, the OEDs of void voxels in a large digital porous medium can be obtained by determining the OEDs of void voxels in each subdomain. Obviously, the OED of a void voxel, determined only in a subdomain, may differ from the OED of the same void voxel determined across the entire domain of the digital porous medium of interest. This discrepancy arises because the accessible solid voxels for a void voxel are more extensive in the whole domain than those in each individual subdomain. On the other hand, it should be noted that not all solid voxels in the entire domain of the digital porous medium of interest are accessible to a given void voxel. Solid voxels located far away from a void voxel may not be accessible. Therefore, for accurate and efficient determination of the OED of a void voxel in a subdomain, we introduce a protective layer surrounding each subdomain. This protective layer ensures enough supply of accessible solid voxels to each void voxel in the subdomain, as illustrated in Fig. 7(b). The protective layer of a subdomain is the zone inside the digital porous medium of interest and adjacent this subdomain. This zone, composed of a subdomain and its protective layer, takes the form of a cuboid. Note that the four subdomains shown in Fig. 7(a) are all attached to the boundary of the digital porous medium. If a face of a subdomain is situated at the boundary of the digital porous medium, then that face of the subdomain is not covered by a protective layer, as illustrated in Fig. 7(b). Conversely, if a subdomain is positioned inside (not at the boundary) of a digital porous medium, then all faces of this subdomain are covered by a protective layer, as illustrated in Fig. S5 in the Supplemental Material [54].

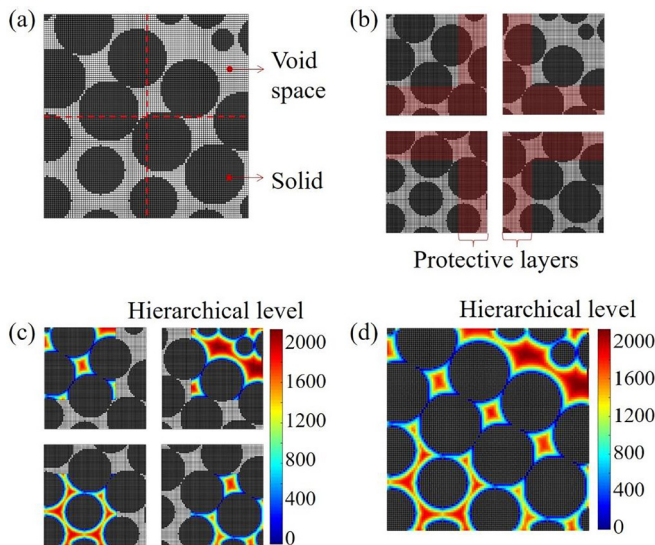


FIG. 7. Schematic of the domain decomposition method to calculate the omnidirectional Euclidean distance (OED) map of a large porous material. (a) A large two-dimensional (2D) digital porous material of 100×100 voxels and four subdomains. (b) Protective layers of subdomain (shown in red). (c) Hierarchical levels of void voxels in subdomains. (d) Hierarchical levels of void voxels in the whole domain.

In this way, we can get the OEDs of void voxels in each subdomain of a digital porous medium, as illustrated Fig. 7(c). For clarity, protective layers are not shown in this figure. By combining the information from the subdomains, the OEDs of void voxels in the whole digital porous medium can be obtained, see Fig. 7(d). It should be noted that the OEDs of void voxels in a subdomain depend on the thickness of the protective layer adjacent to that specific subdomain, as illustrated in Fig. S6 in the Supplemental Material [54]. When the thickness of the protective layer of a subdomain exceeds a critical value, the OEDs of void voxels in this subdomain remain unchanged with the further increase of the thickness of the protective layer. Consequently, the OEDs of void voxels determined through the domain decomposition method align with those determined directly from the whole domain of the digital porous medium of interest.

The domain decomposition method mentioned above aims to determine the OEDs of void voxels and MAs in each subdomain of the digital porous medium of interest. Once the MAs in each subdomain are obtained, they are then consolidated to derive the MAs of the entire domain. From these complete MAs, the extraction of pore throats, pore bodies, and corners in each pore becomes possible. Thus, the accuracy of determining MAs in each subdomain is critical for the effectiveness of the domain decomposition method. If the thickness of the protective layer for each subdomain is sufficiently large (exceeding a critical thickness), the MAs in each subdomain are accurate, and they can seamlessly connect to the MAs in adjacent subdomains. Nevertheless, if the protective layer of a subdomain is insufficient in thickness, redundancies and/or discontinuities in MAs may occur at the interface between two adjacent subdomains, as illustrated in Fig. S7 in the Supplemental Material [54]. This can lead to errors in the extraction of the pore-corner network.

Based on the approach mentioned above, we extract the pore-corner network of a real porous material composed of packed glass beads with a mean diameter of 0.8 mm. The glass bead packing (also called sphere packing) is digitalized to gain the 3D binary image thanks to microcomputed tomography (micro-CT) techniques (see Sec. VI A for more details). The 3D digital image is shown in Fig. 8(a), which has $500 \times 500 \times 400$ voxels (each voxel has a side length of $16.4 \mu\text{m}$). This 3D image is divided into several subdomains, each of which has $50 \times 50 \times 50$ voxels. Each subdomain

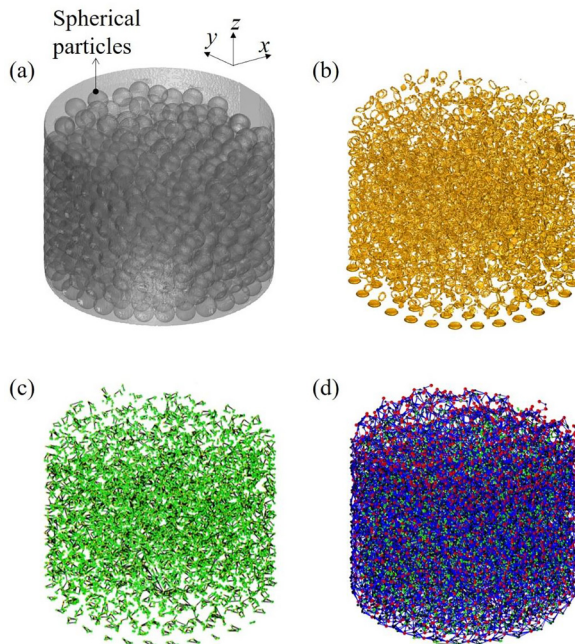


FIG. 8. Schematic of pore-corner-network extraction from a real porous medium composed of packed spheres. (a) Three-dimensional (3D) binary image of the sphere packing obtained by micro-CT techniques. (b) Corners in the sphere packing. (c) Corner network of the sphere packing. (d) Extracted pore-corner network of the sphere packing.

is covered by a protective layer. The effects of the thickness of the protective layer on the extracted MAs are checked. We find that the thickness of 20 voxels is enough for the protective layer and hence is employed for the pore-corner-network extraction shown in Fig. 8. Figure 8(b) shows the corners in the sphere packing, and Fig. 8(c) shows the extracted corner network. The extracted pore-corner network is presented in Fig. 8(d). In this figure, the small red and black spheres represent the centers of pore bodies and pore throats, respectively. The blue lines denote connection between pore bodies. The small green spheres represent the centers of corners within pore bodies, while the small yellow spheres depict the centers of corners within pore throats. The black lines denote connection between pore corners. For clarity, the part of extracted pore-corner network is magnified in Fig. S8 in the Supplemental Material [54]. Such pore-corner-network extraction requires an overall CPU time of ~ 300 h when conducted on a laptop equipped with an i5-8265U processor and 8 GB of RAM. The extraction efficiency can be further improved through the exploration of parallel computing techniques, which will be detailed in a future study. The proposed pore-corner-network extraction method is employed in the following section for the model of evaporation in the sphere packing.

VI. VALIDATION OF THE PROPOSED EXTRACTION METHOD

Since there is no accurate definition of corners within a pore, the extracted corners exemplified by those depicted in Fig. 8(b) cannot be straightforwardly validated through direct comparison with micro-CT images depicted in Fig. 8(a). On the other hand, it is important to note that corners in porous media play an important role in processes such as two-phase transport, particularly in scenarios like evaporation. In the context of evaporation in porous media, the process involves the gradual intrusion of gas into initially liquid-filled pores. As this gas invasion progresses, liquid can be retained within the corners, giving rise to the formation of what are known as corner liquid films.

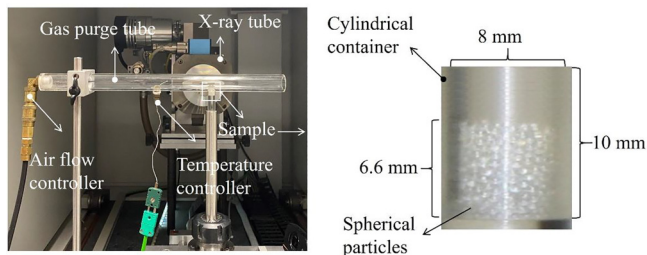


FIG. 9. Experimental setup for evaporation of sphere packing used in the micro-CT experiment.

These corner liquid films hold critical role in dictating the kinetics of evaporation. The morphologies of these corner liquid films, to some extent, represent the topologies of corners.

Thus, the proposed pore-corner-network extraction method put forth in this paper can be validated by comparing the outcomes of modeling and experimentation concerning the dynamic distribution of liquid, particularly the presence and behavior of corner liquid films, within porous media during evaporation. Following this idea, we develop a GNM for evaporation in the sphere packing shown in Fig. 8(a). The experimental data (used for validation) regarding the liquid distribution in the sphere packing are obtained thanks to micro-CT techniques. The micro-CT experiment and the GNM are detailed in the following paragraphs.

A. Micro-CT experiment

A micro-CT experiment is performed to gain the variation of liquid distribution in the sphere packing shown in Fig. 8(a) during evaporation. The sphere packing is placed in a cylindrical transparent container made of plastic (PMMA). The cylindrical container has an inner diameter of 8 mm and a height of 10 mm. The container is vertically placed, and its top is exposed to a horizontally placed gas purge tube with an inner diameter of 16 mm, as illustrated in Fig. 9. The gas purge tube is drilled with a hole of 11.2 mm to connect the top of the cylindrical container.

Initially, the sphere packing in the cylindrical container is saturated with liquid water. Then the drying air with temperature of 26 °C and relative humidity of 40% is flowed into the gas purge tube at the velocity of 1 m/s. In the experiment, the container is placed between the x-ray source and the detector in the micro-CT device. The x-ray cone beam source is generated at an acceleration voltage of 90 kV and a current of 120 μ A by the x-ray source. Then the container is rotated slowly, and 400 different projections, each with an exposure time of 1 ms, are acquired by the detector to reconstruct a 3D CT image. The container is periodically exposed to evaporation and scanning with an average duration of \sim 30 and 25 min, respectively, until it is not feasible to resolve changes in the saturation. The image scanned by x-ray micro-CT device only considers the region of interest; the actual size is $8.2 \times 8.2 \times 6.6$ mm. The corresponding digital image size is $500 \times 500 \times 400$ in this paper. The details of the micro-CT experiment can be found in Ref. [31].

B. GNM

As previously mentioned, we validate our proposed pore-corner-network extraction method by comparing the modeling and experimental results on variation of the liquid distribution in the sphere packing [Fig. 8(a)] during evaporation. The modeling results are derived from the GNM developed based on the pore-corner-network extraction method mentioned above. Thus, it is needed to ensure that the algorithm governing the gas-liquid two-phase transport processes during evaporation in the GNM is accurate enough. This accuracy is vital to mitigate any potential influences stemming from uncertainties in the two-phase transport algorithm. In our previous studies [30], we have developed a model that accounts for continuous and discontinuous corner liquid films. This model can accurately depict the variation of liquid distribution in a microfluidic pore network during

evaporation. Building upon this work, we employ the following procedure to simulate gas-liquid two-phase transport in the sphere packing shown in Fig. 8(a) during evaporation: (1) The liquid saturation in the pore-corner network of the sphere packing is initialized; (2) the vapor pressure field in the sphere packing and the adjacent diffusion boundary layer is determined; (3) the liquid pressure field and the moving menisci, i.e., gas-liquid interfaces, in the extracted pore-corner network of the sphere packing are determined; (4) the time step is determined; (5) the liquid saturation is updated; (6) the steps (2)–(5) are repeated until the total liquid saturation in the sphere packing is decreased to 0.03, which is the total liquid saturation of the last image obtained in the micro-CT experiment. These steps are detailed in the following paragraphs.

For the pore-corner extraction method introduced in the forgoing sections, the corners in a pore unit are determined based on the smallest corner radius of the pore throat in that pore unit. Corners represent the regions occupied by the nonwetting fluid after the complete drainage of the pore unit, wherein both the pore body and all the pore throats are invaded by the nonwetting fluid. By contrast, during the evaporation of the sphere packing in Fig. 8(a), only one liquid-filled pore is invaded at a given time step in a liquid cluster (further explanation is provided below). Thus, the morphologies of corner liquid films in a liquid cluster are dependent on the structure of the pore being invaded by the gas phase, as illustrated in Fig. S9 in the Supplemental Material [54]. In addition, when a pore is filled with liquid, there is no need to consider corner liquid films in that pore. The consideration of corner liquid films mainly stems from the fact that these films in gas-invaded pores can serve as pathways for liquid flow. Thus, in the following paragraphs, the reference to corner liquid films pertains specifically to those in a pore invaded by the gas phase.

Based on the considerations outlined above, the following method is employed to determine corner liquid films in the GNM for the evaporation of porous media. A liquid cluster, with corner liquid films and liquid-filled pores, is considered. Within this liquid cluster, a pore is being invaded by the gas phase, and as a result, corner liquid films are formed in this pore during the invasion process. The morphologies of these corner liquid films within the liquid cluster are determined using the sweeping approach (mentioned earlier) with the corner radius of the pore being invaded. Thus, in our GNM for the evaporation of the sphere packing in Fig. 8(a), the corners in the packing sphere are not predetermined. Instead, the morphologies of corner liquid films in each liquid cluster at each time step are dynamically updated based on the corner radius of the pore being invaded by the gas phase.

In the micro-CT experiment, the sphere packing is located inside a cylindrical tube partially saturated with liquid water. The tube is vertically placed, and the open surface is at the top side. Initially, the sphere packing is completely immersed in liquid water. The gas-liquid interface above the sphere packing is spherical (concave) and moves toward the sphere packing during evaporation, as illustrated in Fig. S10(a) in the Supplemental Material [54]. Because of the shape of this gas-liquid interface above the sphere packing, when gas touches the sphere packing, liquid above the sphere packing is not removed completely; see Fig. S10(b) in the Supplemental Material [54]. At the moment the liquid above the sphere packing is completely removed, some pores in the sphere packing have been occupied by gas, Fig. S10(c) in the Supplemental Material [54]. Since we are concerned on evaporation inside sphere packing, the moment the liquid above the sphere packing is completely removed is taken as the initial moment. The micro-CT experiment indicates that the total liquid saturation S_t is ~ 0.77 at this initial moment. Thus, in the GNM, not all pores are full of liquid initially. The initial liquid saturation in our GNM is determined according to the liquid distribution in the sphere packing at $S_t = 0.77$ obtained in the micro-CT experiment.

In the GNM, the vapor pressure field therein needs to be determined. The vapor pressure field determines the evaporation rate and hence the gas invasion rate of each liquid cluster. The gas invasion in each liquid cluster, on the other hand, controls the liquid distribution. Thus, to avoid any uncertainty of the liquid distribution induced by determination of the vapor pressure field, the vapor pressure field needs to be computed accurately. In previous pore-network models with cuboid pores (the pore corners are hence regular), vapor transport in a cuboid pore with corner liquid films are depicted by a 1D + 1D model, e.g., Ref. [22]. It has been revealed that such a 1D + 1D model

is not accurate, even for cuboid pores [30]. In our extracted pore-corner network, the pores and corners are irregular, implying that vapor transport in these pores cannot be depicted accurately by the 1D + 1D model. For this reason, we use the finite volume method to solve the vapor diffusion equation to calculate the vapor pressure in each void voxel full of gas in the sphere packing. Here, a pore, corner, or void voxel fully filled with gas means that it is filled by gas; a liquid-filled pore, corner, or void voxel means that it is partially or fully filled with liquid. For the evaporation process explored here, liquid is the wetting fluid, and gas is the nonwetting fluid. The vapor diffusion is considered a quasisteady process and hence is described by $\nabla \cdot \left(\frac{DP_g}{RT} \frac{1}{P_g - P_v} \nabla P_v \right) = 0$. Here, D is the vapor diffusion coefficient ($1.264 \times 10^{-5} \text{ m}^2/\text{s}$), R the gas constant ($8.314 \text{ J mol}^{-1} \text{ K}^{-1}$), T the gas temperature (26°C), P_g the total gas pressure ($1.013 \times 10^5 \text{ Pa}$), and P_v the partial vapor pressure.

In the calculation of the vapor pressure field, the vapor pressure of each void voxel with liquid is equal to the saturation vapor pressure, and the vapor pressure at the outlet of the tube containing the packing sphere is determined by the ambient temperature (26°C) and relative humidity (40%). The solid void pixel is nonpermeable to vapor diffusion. The void region between the top of sphere packing and the outlet of cylindrical tube is also divided into several mesh elements. The sizes of these mesh elements in the x and y directions are equal to those of voxels in the sphere packing. Thus, at the interface between this void region and the sphere packing, each voxel is in contact with a mesh element with an edge length of $16.4 \mu\text{m}$. In the z direction, there are 15 mesh elements in the void region. For the first 5 layers of mesh close to the sphere packing, the mesh elements have a side length of $20 \mu\text{m}$ along the z direction, while the remaining 10 mesh elements have a side length of 0.33 mm along this direction. Based on these mentioned sizes of mesh elements and boundary conditions, the vapor pressure field in the sphere packing can be obtained by solving the steady vapor diffusion equation mentioned above.

We find that, even at the total liquid saturation of 0.03 (the final moment in our GNM), the void voxels full of gas from the first to the 380th voxel slice in the z direction have a vapor pressure equal to the saturated one even with a thin diffusion layer at the top of sphere packing; see Fig. S11 in the Supplemental Material [54]. The sphere packing has 400 voxel slices, each of which has only one voxel, along the z direction. The first slice is at the bottom, whereas the last one is at the top of sphere packing. In these void voxels full of gas from the first to the 380th voxel slice, vapor is always saturated when the total liquid saturation is >0.03 . For this reason, the vapor pressures in these void voxels are set to be the saturated one, and only the vapor pressures in void voxels full of gas in the 20 voxel slices adjacent to the top of sphere packing are calculated in our GNM to save the computational time.

After the vapor pressure field is obtained, then the evaporation rate from each liquid cluster can be determined, from which evaporation-induced gas invasion is determined. The evaporation rate from the sphere packing is rather small, which in turn results in a low capillary number. The capillary number C_a represents the ratios of the viscous to the capillary forces, which can be determined by the equation $C_a = \frac{\mu_l Q}{A \sigma \rho_l}$. Here, μ_l is the liquid viscosity (0.001 Pa s), Q the mass flow at the initial moment of evaporation ($1.1 \times 10^{-8} \text{ kg/s}$), A the area of cross-section of porous media ($6.4 \times 10^{-5} \text{ m}^2$), σ the liquid surface tension (0.0728 N/m), and ρ_l the liquid density (995 kg/m^3). Hence, the calculated capillary number is 2.3×10^{-9} . Evaporation-induced gas invasion in the sphere packing can be considered a quasistatic process. To this end, for a liquid cluster with liquid-filled pores and corner liquid films, only the available liquid-filled pore with the lowest threshold pressure will be invaded by gas at each step. Here, an available liquid-filled pore is the one adjacent to at least a pore invaded by gas. The threshold pressure for gas to invade a liquid-filled pore throat is defined as the one for invasion of a nonwetting fluid into the cross-section at the center of this pore throat and perpendicular to the MA (see Sec. IV for more details). The value of contact angle is needed to determine the threshold pressure. The contact angle taken in the liquid phase is assumed to be zero. A pore body has a larger size than its adjacent pore throats. Thus, once a pore throat with liquid is invaded by gas, its adjacent liquid-filled pore body will be invaded subsequently. For this reason, the threshold pressure for gas to invade a liquid-filled pore body is taken as the smallest threshold

pressure of the pore throats full of gas adjacent to this pore body. Since we assume that the contact angle is zero, the capillary valve effect due to sudden geometrical expansion can be neglected; see Ref. [59] for detailed explanation.

Since corners occupied by liquid have a smaller size and hence a higher threshold pressure than pores, liquid-filled corners in a liquid cluster will be the last to be invaded by gas. A liquid-filled corner can be invaded only in a liquid cluster without liquid-filled pores, i.e., in a liquid cluster composed of only liquid-filled corners. As the amount of liquid in a corner reduces, the curvature radius of the gas-liquid interface in this corner decreases, thereby leading to the reduced liquid pressure (if the gas pressure is assumed constant), and hence, the flow of liquid into this corner from other corners in the same liquid cluster. Thus, for a liquid cluster composed of only the liquid-filled corners, the amount of liquid in all corners will be reduced during evaporation, and the liquid-filled corners are not emptied one by one. On the other hand, at each time step, the morphologies of corner liquid films in each liquid cluster containing liquid-filled pores are updated based on the corner radius of the pore with a moving meniscus.

Thus, for evaporation of the sphere packing, the progression is such that solely the pore with the lowest threshold pressure available is invaded by gas. This pore contains a moving gas-liquid interface, or meniscus, within a cluster of interconnected liquid-filled pores. The duration required to empty this specific pore is equal to the mass of liquid it accommodates and the decreased mass of corner liquid films divided by the evaporation rate associated with the corresponding liquid cluster. The reduction in the mass of corner liquid films in a liquid cluster is equal to the difference between the mass of corner liquid films at the last time step and the mass at the current time step. For a liquid cluster composed of only liquid-filled corners, all the menisci within these corners are moving, and the time to empty these corners is equal to the mass of liquid in these corners divided by the evaporate rate of this liquid cluster. The time step is the minimum time to empty a pore or a corner cluster in each liquid cluster. Based on this time step, the liquid saturations in the pores and corners containing moving menisci are updated.

C. Comparison

The comparison between the modeling outcomes derived from GNM and the data acquired through micro-CT experimentation for evaporation of sphere packing shown in Fig. 8(a) is presented in Figs. 10–12. Figure 10 shows the liquid distribution profile within the sphere packing, traversing the z direction (thickness direction) at various total liquid saturations. This profile is generated by segmenting the sphere packing into 40 layers along the z direction, with each layer encompassing 10 voxels in the z direction. The liquid saturation in each layer S_l is obtained based on the liquid volume and the volume of void space in this layer. The horizontal axis in Fig. 10 is the fractional distance f equal to the distance from the layer to the bottom of sphere packing divided by the length of sphere packing along the z direction. Figure 11 shows the distributions of liquid in the sphere packing at various total liquid saturation. For clarity, the solid phase is not shown in this figure. The liquid is shown in blue in the experimental data and red in the modeling results. The distributions of liquid in the voxel slices along the z direction are shown in Figs. S12–S15 in the Supplemental Material [54]. There are 400 voxel slices along the z direction, each of which has only one voxel in the z direction. The first voxel slice is positioned at the bottom, while the last one is at the top of the sphere packing. Figure 12 shows the variation of the total liquid saturation in the sphere packing over the course of evaporation. Overall, the modeling and experimental results are in good agreement, demonstrating the effectiveness of the proposed method for extracting pore-corner networks.

As illustrated in Fig. 10, the regions of spheres packing at $f < 0.8$ are fully saturated with liquid at the total liquid saturation of 0.77, indicating that, when $S_l > 0.77$, evaporation-induced gas invasion occurs only near the open surface of the sphere packing. At the total liquid saturation of 0.52, the liquid saturation at the bottom of the sphere packing is smaller than 1, indicating that gas percolates through the sphere packing. At $S_l = 0.52$, the liquid saturation near the open surface is trivial, not more than 0.04, and the liquid resides mainly in the corners in zone near the open

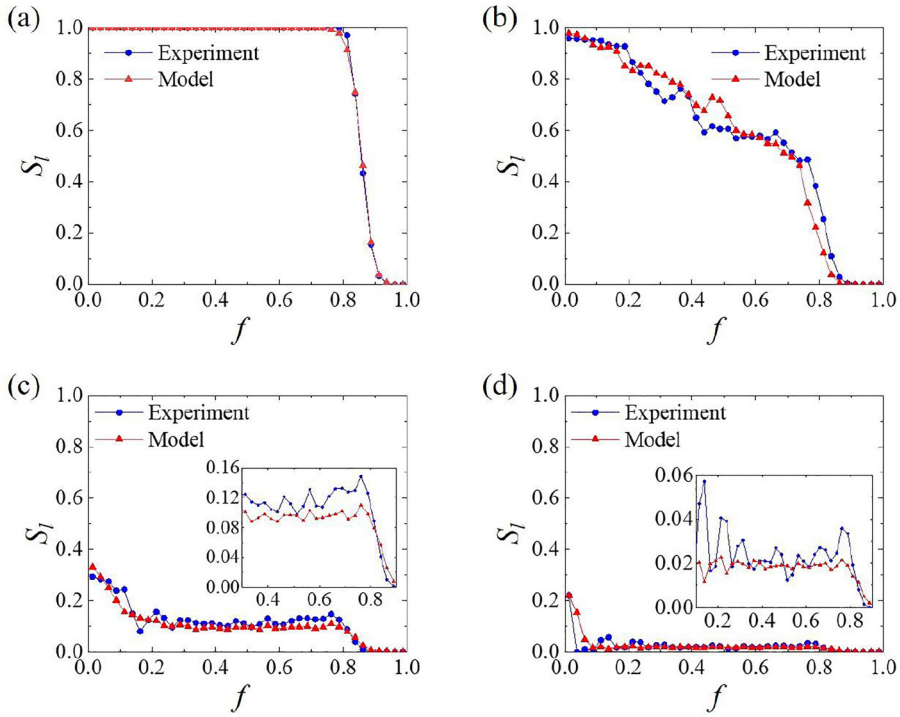


FIG. 10. Liquid distribution profile in the sphere packing along the z direction, obtained from micro-CT experiment and generalized network model (GNM) simulation, at total liquid saturations of (a) 0.77, (b) 0.52, (c) 0.10, and (d) 0.03.

surface, as indicated by the liquid distribution in the 350th voxel slice shown in Fig. S13 in the Supplemental Material [54]. At a total liquid saturation of 0.1, the liquid saturation profile at $0.2 < f < 0.8$ is flattened. As the total liquid saturation reduces to 0.03, liquid resides mainly in the corners, and the liquid saturation is zero for $f > 0.9$.

To elucidate the role of corner liquid films, we also present the liquid saturation profiles obtained using the GNM without corner liquid films in Fig. S16 in the Supplemental Material [54]. In the

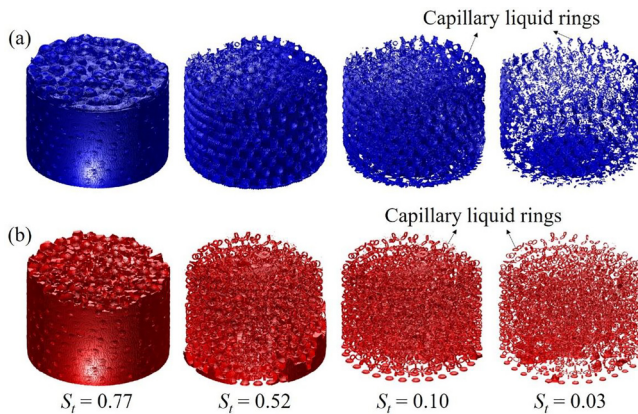


FIG. 11. Distributions of liquid in the sphere packing at various total liquid saturations S_t obtained from (a) micro-CT experiment and (b) generalized network model (GNM) simulation.

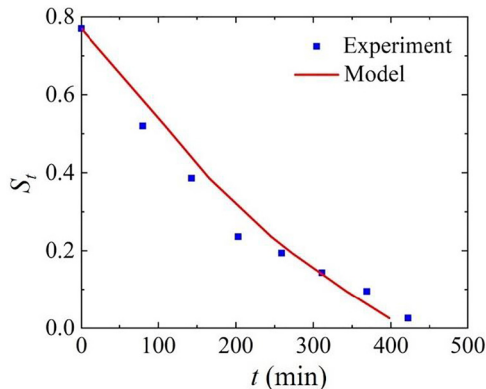


FIG. 12. Variation of the total liquid saturation S_t in the packing sphere with evaporation time t obtained from micro-CT experiment and generalized network model (GNM) simulation.

GNM without corner liquid films, the pore network extracted from the sphere packing shown in Fig. 8(a) is employed. When the corner liquid films are not considered in the GNM, the simulated liquid saturation profile deviates from the experimental data, as depicted in Fig. S16 in the Supplemental Material [54]. For instance, at a total liquid saturation of 0.6, the liquid saturation at the bottom of the packing sphere is ~ 0.3 ; however, the GNM without corner liquid films indicates a value of 0.6.

Note that some differences can be observed between the experimental data and the modeling results from GNM with corner liquid films. The main reason could be owing to the digitalization of the sphere packing. The digital image of the sphere packing obtained from the micro-CT is composed of voxels which are either solid or void. The accuracy of the digital image depends on voxel size. The smaller the voxel size is, the more accurate the digital image. However, the view field of the image obtained from micro-CT decreases with the smaller voxel size. To capture the whole sphere packing, the cubic voxel has a side length of $16.4 \mu\text{m}$ in this paper. Apparently, such voxelization shall result in error in determining the sizes of pore corners and the threshold pressures of the pore throats, thereby leading to the error in modeling the evaporation-induced gas invasion in the extracted pore-corner network. In addition, even though the evaporation rate is rather small, neglecting the effect of liquid viscosity, especially on the liquid flow in the pore corners, could also result in the difference between the modeling and experimental results. Finally, in the micro-CT experiment, a CT image is acquired every 55 min, including 30 min waiting time and 25 min scanning time. The liquid saturation is always decreasing during the 25 min scanning process, causing the error in determination of the volume of liquid.

Despite the differences between the modeling predictions and the experimental results, the corner liquid films revealed in the experiment are also successfully replicated by the proposed model; see the corner liquid films in the 350th voxel slice in Fig. S15 in the Supplemental Material [54]. The results indicate that the positions of corner liquid films in the model results are in good agreement with that in the experimental data. Furthermore, the model effectively captures the formation of capillary liquid rings, attributed to the presence of corner liquid films, which are observed in the experiment, as depicted in Fig. 11. Since the corner liquid films reside in corners, the agreement in the distribution of corner liquid films between the model and experiment further demonstrates the validity and effectiveness of the pore-corner-network extraction method proposed in this paper.

VII. CONCLUSIONS

In this paper, we propose a method to extract and examine the intricate pore-corner networks residing in porous media. These networks serve as a fundamental building block for the development

of GNMs. The proposed extraction process consists of two sequential steps. First, the extraction focuses on the pore networks, which are comprised of pore bodies interconnected by pore throats. This step utilizes the OED concept. Second, the corners within each distinct pore unit, formed by a pore body and half of the connected pore throats, are determined by sweeping the pore unit with a sphere. The radius of the sphere is determined as the minimal corner radius for the cross-sections at the centers of pore throats within the pore unit. Once the corners within each pore unit are identified in this way, the resulting pore-corner network is subsequently established.

To validate our proposed extraction method, we simulate evaporation of a model porous medium composed of packed spherical beads based on our proposed pore-corner-network extraction method. We then compare our simulation results with data gained from micro-CT experiments, specifically focusing on the variations in the liquid distribution during evaporation. The liquid distributions and the variation of total liquid saturation with time obtained from both the model and the micro-CT experiment exhibit remarkable congruence. Notably, the experimentally observed capillary rings, formed by liquid accumulation in corners, are captured in our model. These consistent findings between our modeling approach and experimental observations provide evidence for the efficacy of our proposed method in accurately extracting pore-corner networks that truly represent the intricate pore structure of porous media.

The proposed extraction method serves as a valuable tool for characterizing the intricate structures of pore and corners within porous media. This method offers a quantitative means to investigate the interplay between fabrication parameters and the structures of pores and corners in industrial porous materials, such as gas diffusion layers in proton exchange membrane fuel cells. Determination of such quantitative relationships is of vital importance as it facilitates the optimization of fabrication protocols for porous materials.

Moreover, the utilization of the extracted pore-corner networks in the development of a GNM unveils the pivotal role of corner films in multiphase-phase transport in porous media, offering a granular insight into pore-scale phenomena. This revelation enhances the understanding of the multiphase-phase transport mechanisms in porous media, thus propelling the development of continuum models.

From these points of view, the pore-corner extraction method proposed in this paper not only contributes to reveal the structures of pores and corners in porous media but also brings benefits to the development of continuum models aimed at comprehending multiphase transport phenomena in porous media.

ACKNOWLEDGMENTS

The authors are grateful for the support of the National Key Research and Development Program of China (Grant No. 2021YFA0717200), the National Science Foundation of China (Grant No. U20B2003), the Sinopec Group Project (Grant No. P21037-4), the Sino-German Center (Grant No. M-0545), the Deutsche Forschungsgemeinschaft (Grant No. 422037413-TRR287), and the Alexander von Humboldt Foundation.

-
- [1] P. Druetta, P. Raffa, and F. Picchioni, Chemical enhanced oil recovery and the role of chemical product design, *Appl. Energy* **252**, 113 (2019).
 - [2] M. Fani, P. Pourafshary, P. Mostaghimi, and N. Mosavat, Application of microfluidics in chemical enhanced oil recovery: A review, *Fuel* **315**, 123 (2022).
 - [3] E. Martin-Roberts, V. Scott, S. Flude, G. Johnson, R. S. Haszeldine, and S. Gilfillan, Carbon capture and storage at the end of a lost decade, *One Earth* **4**, 1569 (2021).
 - [4] S. Krevor, H. de Coninck, S. E. Gasda, N. S. Ghaleigh, V. de Gooyert, H. Hajibeygj, R. Juanes, J. Neufeld, J. J. Roberts, and F. Swennenhuis, Subsurface carbon dioxide and hydrogen storage for a sustainable energy future, *Nat. Rev. Earth Environ.* **4**, 102 (2023).

- [5] K. Jiao, J. Xuan, Q. Du, Z. Bao, B. Xie, B. Wang, Y. Zhao, L. Fan, H. Wang, Z. Hou *et al.*, Designing the next generation of proton-exchange membrane fuel cells, *Nature (London)* **595**, 361 (2021).
- [6] S. Yuan, C. Zhao, X. Cai, L. An, S. Shen, X. Yan, and J. Zhang, Bubble evolution and transport in PEM water electrolysis: Mechanism, impact, and management, *Prog. Energy Combust. Sci.* **96**, 101 (2023).
- [7] R. Wu, A. Kharaghani, and E. Tsotsas, Two-phase flow with capillary valve effect in porous media, *Chem. Eng. Sci.* **139**, 241 (2016).
- [8] R. Wu, C. Y. Zhao, E. Tsotsas, and A. Kharaghani, Convective drying in thin hydrophobic porous media, *Int. J. Heat Mass Transfer* **112**, 630 (2017).
- [9] T. Zhang, R. Wu, C. Y. Zhao, E. Tsotsas, and A. Kharaghani, Capillary instability induced gas-liquid displacement in porous media: Experimental observation and pore network model, *Phys. Rev. Fluids* **5**, 104305 (2020).
- [10] A. Q. Raeini, Modelling two-phase flow in porous media at the pore scale using the volume-of-fluid method, *J. Comput. Phys.* **231**, 56 (2012).
- [11] S. Li, H. Liu, R. Wu, J. Cai, G. Xi, and F. Jiang, Prediction of spontaneous imbibition with gravity in porous media micromodels, *J. Fluid Mech.* **952**, A9 (2022).
- [12] K. M. Waananen, J. B. Litchfield, and M. R. Okos, Classification of drying models for porous solids, *Drying Technol.* **11**, 1 (1993).
- [13] A. Q. Raeini, B. Bijeljic, and M. J. Blunt, Generalized network modeling: Network extraction as a coarse-scale discretization of the void space of porous media, *Phys. Rev. E* **96**, 013312 (2017).
- [14] R. Wu and C. Y. Zhao, Distribution of liquid flow in a pore network during evaporation, *Phys. Rev. E* **104**, 025107 (2021).
- [15] M. Hashemi, B. Dabir, and M. Sahimi, Dynamics of two-phase flow in porous media: Simultaneous invasion of two fluids, *AIChE J.* **45**, 1365 (1999).
- [16] M. Moura, E. G. Flekkoy, K. J. Maloy, G. Schafer, and R. Toussaint, Connectivity enhancement due to film flow in porous media, *Phys. Rev. Fluids* **4**, 094102 (2019).
- [17] B. K. Primkulov, A. A. Pahlavan, X. Fu, B. Zhao, C. W. MacMinn, and R. Juanes, Wettability and Lenormand's diagram, *J. Fluid Mech.* **923**, A34 (2021).
- [18] H. Geistlinger, Y. Ding, B. Apelt, S. Schluter, M. Kuchler, D. Reuter, N. Vorhauer, and H. J. Vogel, Evaporation study based on micromodel experiments: Comparison of theory and experiment, *Water Resour. Res.* **55**, 6653 (2019).
- [19] S. C. Iden, J. R. Blocher, E. Diamantopoulos, and W. Durner, Capillary, film, and vapor flow in transient bare soil evaporation (1): Identifiability analysis of hydraulic conductivity in the medium to dry moisture range, *Water Resour. Res.* **57**, e2020WR028513 (2021).
- [20] R. Wu and F. Chen, Interplay between salt precipitation, corner liquid film flow, and gas-liquid displacement during evaporation in microfluidic pore networks, *J. Appl. Phys.* **133**, 074701 (2023).
- [21] A. G. Yiotis, A. G. Boudouvis, A. K. Stubos, I. N. Tsimpanogiannis, and Y. C. Yortsos, Effect of liquid films on the isothermal drying of porous media, *Phys. Rev. E* **68**, 037303 (2003).
- [22] A. G. Yiotis, A. G. Boudouvis, A. K. Stubos, I. N. Tsimpanogiannis, and Y. C. Yortsos, Effect of liquid films on the drying of porous media, *AIChE J.* **50**, 2721 (2004).
- [23] L. A. Segura and P. G. Toledo, Pore-level modeling of isothermal drying of pore networks. Effects of gravity and pore shape and size distributions, *Chem. Eng. J.* **111**, 237 (2005).
- [24] A. G. Yiotis, A. K. Stubos, A. G. Boudouvis, I. N. Tsimpanogiannis, and Y. C. Yortsos, Pore-network modeling of isothermal drying in porous media, *Transp. Porous Media* **58**, 63 (2005).
- [25] M. Prat, On the influence of pore shape, contact angle and film flows on drying of capillary porous media, *Int. J. Heat Mass Transfer* **50**, 1455 (2007).
- [26] A. G. Yiotis, I. N. Tsimpanogiannis, A. K. Stubos, and Y. C. Yortsos, Coupling between external and internal mass transfer during drying of a porous medium, *Water Resour. Res.* **43**, W06403 (2007).
- [27] M. Prat, Pore network models of drying, contact angle, and film flows, *Chem. Eng. Technol.* **34**, 1029 (2011).
- [28] N. Vorhauer, Y. J. Wang, A. Kharaghani, E. Tsotsas, and M. Prat, Drying with formation of capillary rings in a model porous medium, *Transp. Porous Media* **110**, 197 (2015).

- [29] S. Lal, M. Prat, M. Plamondon, L. Poulikakos, M. N. Partl, D. Derome, and J. Carmeliet, A cluster-based pore network model of drying with corner liquid films, with application to a microporous material, *Int. J. Heat Mass Transfer* **140**, 620 (2019).
- [30] R. Wu, T. Zhang, C. Ye, C. Y. Zhao, E. Tsotsas, and A. Kharaghani, Pore network model of evaporation in porous media with continuous and discontinuous corner films, *Phys. Rev. Fluids* **5**, 014307 (2020).
- [31] A. Kharaghani, H. T. Mahmood, Y. Wang, and E. Tsotsas, Three-dimensional visualization and modeling of capillary liquid rings observed during drying of dense particle packings, *Int. J. Heat Mass Transfer* **177**, 121505 (2021).
- [32] F. Chauvet, P. Duru, S. Geoffroy, and M. Prat, Three periods of drying of a single square capillary tube, *Phys. Rev. Lett.* **103**, 124502 (2009).
- [33] F. Chauvet, P. Duru, and M. Prat, Depinning of evaporating liquid films in square capillary tubes: Influence of corners' roundedness, *Phys. Fluids* **22**, 664 (2010).
- [34] D. Silin and T. Patzek, Pore space morphology analysis using maximal inscribed spheres, *Physica A* **371**, 336 (2006).
- [35] A. S. Al-Kharusi and M. J. Blunt, Network extraction from sandstone and carbonate pore space images, *J. Pet. Sci. Eng.* **56**, 219 (2007).
- [36] N. Zhan, R. Wu, E. Tsotsas, and A. Kharaghani, Proposal for extraction of pore networks with pores of high aspect ratios, *Phys. Rev. Fluids* **7**, 014304 (2022).
- [37] H. Dong and M. J. Blunt, Pore-network extraction from micro-computerized-tomography images, *Phys. Rev. E* **80**, 036307 (2009).
- [38] F. Arand and J. Hesser, Accurate and efficient maximal ball algorithm for pore network extraction, *Comput. Geosci.* **101**, 28 (2017).
- [39] D. Zheng, W. Wang, and Z. Reza, Pore-network extraction algorithm for shale accounting for geometry-effect, *J. Pet. Sci. Eng.* **176**, 74 (2019).
- [40] A. Rabbani, S. Jamshidi, and S. Salehi, An automated simple algorithm for realistic pore network extraction from micro-tomography images, *J. Pet. Sci. Eng.* **123**, 164 (2014).
- [41] T. Agaesse, A. Lamibrac, F. N. Buchi, J. Pauchet, and M. Prat, Validation of pore network simulations of ex-situ water distributions in a gas diffusion layer of proton exchange membrane fuel cells with x-ray tomographic images, *J. Power Sources* **331**, 462 (2016).
- [42] J. T. Gostick, Versatile and efficient pore network extraction method using marker-based watershed segmentation, *Phys. Rev. E* **96**, 023307 (2017).
- [43] A. Rabbani and M. Babaei, Hybrid pore-network and lattice-Boltzmann permeability modeling accelerated by machine learning, *Adv. Water Res.* **126**, 116 (2019).
- [44] A. Rabbani, P. Mostaghimi, and R. T. Armstrong, Pore network extraction using geometrical domain decomposition, *Adv. Water Res.* **123**, 70 (2019).
- [45] Z. A. Khan, A. Elkamel, and J. T. Gostick, Efficient extraction of pore networks from massive tomograms via geometric domain decomposition, *Adv. Water Res.* **145**, 103734 (2020).
- [46] T. Lee and R. L. Kashyap, Building skeleton models via 3D medial surface/axis thinning algorithms, *CVGIP: Graph. Models Image Process.* **56**, 462 (1994).
- [47] W. B. Lindquist and A. Venkatarangan, Investigation 3D geometry of porous media from high resolution images, *Phys. Chem. Earth A* **24**, 593 (1999).
- [48] R. Al-Raoush, K. Thompson, and C. S. Willson, Comparison of network generation techniques for unconsolidated porous media, *Soil Sci. Soc. Am. J.* **67**, 1687 (2003).
- [49] R. I. Al-Raoush and C. S. Willson, Extraction of physically realistic pore network properties from three-dimensional synchrotron x-ray microtomography images of unconsolidated porous media systems, *J. Hydrol.* **300**, 44 (2005).
- [50] Z. Jiang, K. Wu, G. Couples, M. I. J. van Dijke, K. S. Sorbie, and J. Ma, Efficient extraction of networks from three-dimensional porous media, *Water Resour. Res.* **43**, W12S03 (2007).
- [51] Z. Jiang, M. I. J. van Dijke, S. Geiger, J. Ma, G. D. Couples, and X. Li, Pore network extraction for fractured porous media, *Adv. Water Res.* **107**, 280 (2017).

- [52] K. M. Gerke, T. O. Sizonenko, M. V. Karsanina, E. V. Lavrukhin, V. V. Abashkin, and D. V. Korost, Improving watershed-based pore-network extraction method using maximum inscribed ball pore-body positioning, *Adv. Water Res.* **140**, 103 (2020).
- [53] Z. Yi, M. Lin, W. Jiang, Z. Zhang, H. Li, and J. Gao, Pore network extraction from pore space images of various porous media systems, *Water Resour. Res.* **53**, 3424 (2017).
- [54] See Supplemental Material at <http://link.aps.org/supplemental/10.1103/PhysRevFluids.9.014303> for more details on pore-corner network extraction.
- [55] O. I. Frette and J. O. Helland, A semi-analytical model for computation of capillary entry pressures and fluid configurations in uniformly-wet pore spaces from 2D rock images, *Adv. Water Res.* **33**, 846866 (2010).
- [56] J. P. Braquelaire and A. Vialard, Euclidean paths: A new representation of boundary of discrete regions, *CVGIP: Graph. Models Image Process.* **61**, 1643 (1999).
- [57] C. R. Brice and C. L. Fennema, Scene analysis using regions, *Artif. Intell.* **1**, 205226 (1970).
- [58] J. Hoshen and R. Kopelman, Percolation and cluster distribution. I. Cluster multiple labeling technique and critical concentration algorithm, *Phys. Rev. B* **14**, 3438 (1976).
- [59] R. Wu, L. Yang, and C. Y. Zhao, Evaporation from thin porous media with mixed intermediately-wet and hydrophobic networks, *Int. J. Therm. Sci.* **138**, 159 (2019).